remote sensing

Article

Quantitative Assessment of Cropland Exposure to Agricultural Drought in the Greater Mekong Subregion

Wenting Ming [1], Xian Luo [2], Xuan Luo [1], Yunshu Long [1], Xin Xiao [1], Xuan Ji [2] and Yungang Li [2,*]

[1] Institute of International Rivers and Eco-Security, Yunnan University, Kunming 650504, China; mingwt@mail.ynu.edu.cn (W.M.); xuanluo@mail.ynu.edu.cn (X.L.); long_ys@mail.ynu.edu.cn (Y.L.); xiaoxin@mail.ynu.edu.cn (X.X.)

[2] Yunnan Key Laboratory of International Rivers and Transboundary Eco-Security, Yunnan University, Kunming 650504, China; luoxian@ynu.edu.cn (X.L.); jixuan@ynu.edu.cn (X.J.)

* Correspondence: ygli@ynu.edu.cn

Abstract: Accurate and reliable information on the spatiotemporal characteristics of agricultural drought is important in understanding complicated drought processes and their potential impacts. We proposed an integrated approach for detecting agricultural droughts and their cropland exposure using remote sensing data over the Greater Mekong Subregion (GMS) collected from 2001 to 2020. The soil moisture (SM) dataset (0.05°) was first reconstructed based on an ESACCI SM dataset using a random forest (RF) model. Subsequently, the standardized soil moisture index (SSMI) was used to identify the agricultural droughts by a three-dimensional (latitude-longitude-time) identification method. In addition, the cropland's exposure to agricultural droughts was evaluated. Results showed that: (1) the reconstructed SM data achieved spatial continuity and improved spatial resolution. The verified consequences showed that the reconstructed SM data agreed well with the in situ SM data. Additionally, the SSMI based on reconstructed SM had good correlations with the standardized precipitation evapotranspiration index (SPEI) calculated from station observations. (2) Twenty agricultural drought events lasting at least 3 months were identified over the GMS region. The averaged durations, areas, and severity were 7 months, 9×10^5 km^2, and 45.6×10^5 month·km^2, respectively. The four worst drought events ranked by severity were the 2019–2020 event, the 2015–2016 event, the 2009–2010 event, and the 2004–2005 event. (3) Based on the 20 identified agricultural drought events, cropland exposure was high in Myanmar, Thailand, and Cambodia. On average, the cropland exposure over the GMS was 1.71×10^5 km^2, which accounts for 34% of the total cropland. Notably, the four severest drought events swept over 80% of the total cropland area. This study enriched our understanding of the development process of agricultural droughts from a space-time perspective, which was pivotal for assessing drought impacts and managing agricultural water resources.

Keywords: agricultural drought; soil moisture data reconstruction; three-dimensional identification; cropland exposure; the Greater Mekong Subregion

Citation: Ming, W.; Luo, X.; Luo, X.; Long, Y.; Xiao, X.; Ji, X.; Li, Y. Quantitative Assessment of Cropland Exposure to Agricultural Drought in the Greater Mekong Subregion. *Remote Sens.* **2023**, *15*, 2737. https://doi.org/10.3390/rs15112737

Academic Editors: Shibo Fang, Lei Wang, Wen Zhuo and Ce Zhang

Received: 19 April 2023
Revised: 20 May 2023
Accepted: 22 May 2023
Published: 24 May 2023

1. Introduction

Drought is a natural hydroclimatic hazard that negatively impacts agricultural production, ecosystems, and the social economy [1,2]. Drought is divided into meteorological, agricultural, hydrological, socioeconomic, and environmental droughts [3,4]. Among them, agricultural drought is a period of soil water deficit due to one or more factors of low precipitation, high evaporation, and transpiration, leading to crop failure [4]. Agricultural drought may occur at any stage of the crop-growing season and reduce crop yields [5]. Given the consequences and pervasiveness of agricultural drought, the accurate identification and monitoring of agricultural drought is critical for agricultural production and food safety [6].

Many drought indices have been proposed to represent agricultural drought based on ground observations and remote sensing [7], for example, those based on meteorological variables: the standardized precipitation index (SPI) and the standardized precipitation evapotranspiration index (SPEI) [4]; those based on soil moisture (SM): the standardized SM index (SSMI) [8] and SM deficit index (SMDI) [9] and those based on vegetation: normalized difference vegetation index (NDVI) and enhanced vegetation index (EVI) [10]. SM affects the changes in water and energy fluxes between land and atmosphere, which is an important limiting factor for crop production and has closer correlations to crop yield reduction. In addition, SM affects vegetation growth more directly than the influence of precipitation [5]. Therefore, SM is considered a key indicator for representing agricultural drought [11].

SM is traditionally obtained from in situ observations, which provide reliable SM estimation. However, it is challenging to express SM in a wide area by a single-point ground observation [12]. Remote sensing could provide spatiotemporally continuous global SM estimation [13]. Currently, satellite sensors such as the Advanced Scatterometer (ASCAT) [14], Soil Moisture Active Passive (SMAP) [15], Soil Moisture Ocean Salinity (SMOS) [16], and Sentinel missions [17] can retrieve global SM. However, most of these sensors commenced their operations after 2005, which cannot be applied to long-term drought research. The European Space Agency Climate Change Initiative (ESACCI) exploited multi-source data with the complete global SM data over 40 years. The dataset combines several SM products from a variety of satellite sensors, making up for the shortcoming of existing SM estimates [18]. The ESACCI SM dataset has been verified in many regions worldwide and has been proven to have similar temporal trends as in the in situ SM [19–21]. Therefore, it is an invaluable data source for agricultural drought monitoring on a global scale or regionally [11,22].

Nevertheless, the ESACCI SM dataset has several limitations in agricultural drought monitoring applications. There are many missing or poor-quality SM values due to factors such as cloud contamination, failure of satellite operation, satellite orbit changes, and uncertainty on the coast and in the mountains [23–25]. Moreover, the ESACCI SM dataset has a spatial resolution of 0.25°, which is coarse to support the applicable conditions in some regional areas. To solve this problem, ESACCI SM filling and reconstructing methods were proposed to increase data integrity and improve spatial resolution [25,26]. The core idea of SM data filling and reconstructing is to institute a statistical or physical relationship between SM and environmental variables. Machine learning (ML) techniques have been recently widely used in SM data reconstruction applications [27,28]. For instance, random forest (RF) has been proven effective because of its excellent capability to reconstruct remote sensing products [29–31].

The identification and feature extraction of droughts is crucial to explore the spatiotemporal variations of drought events. Traditional methods determined the temporal characteristics of drought in specific regions or detected the areal extent affected by droughts over a specific period. However, a drought event is a three-dimensional (3D) phenomenon—it involves both time and space dimensions [32]. Therefore, drought events identified from time-only or spatial-only dimensions usually neglect and discard much of the continuous spatiotemporal property of the actual droughts [33]. Some reports have considered the spatiotemporal synchronous identification and feature extraction of droughts [34]. The representative study of Andreadis, et al. [35] introduced a clustering algorithm that can be used to identify a single drought event through space and time. Lloyd-Hughes [33] extended this method to analyze the resemblance between the structures of individual droughts. Later, a study implemented a technique by gathering contiguous drought regions into clusters worldwide [36]. After that, this spatiotemporal technique was applied to characterizing droughts by several researchers [37–39]. In addition, the 3D approach was used to explore the population exposed to drought events [40]. However, less attention was given to the influence of agricultural droughts on cropland exposure [41,42].

The Greater Mekong Subregion (GMS) includes Cambodia, Laos, Myanmar, Thailand, Vietnam, and the Yunnan Province of China. The population of the region was approximately 295 million in 2021. Approximately 70% of the population in the Lower Mekong Basin is active in agriculture [43]. Under the context of global warming, droughts are becoming frequent and severe in the region. For example, droughts in 1997–1998, 2003–2005, 2009–2010, 2015–2016, and 2019–2020 caused severe impacts on agricultural production [1,44–46]. Former studies of droughts over the GMS mainly involved meteorological and hydrological droughts [1,47–49]. To the best of our knowledge, few studies have used long-term and high-resolution SM data to monitor agricultural drought and cropland exposure in the drought-vulnerable GMS. Overall, the primary goals of this study can be summarized as follows: (1) to reconstruct a high spatial resolution (0.05°) SM dataset based on the ESACCI data; (2) to identify the agricultural drought characteristics from 3D identification method and (3) to explore the cropland's exposure to agricultural drought in the last two decades. The contribution of our research is to use high spatial resolution SM data to identify agricultural drought events from a perspective of a three-dimensional (latitude-longitude-time) and reveal the exposure of the cropland to drought events, which is pivotal for assessing drought impacts and managing agricultural water resources.

2. Materials and Methods

2.1. Study Area

The GMS geographically consists of Yunnan in China and five countries in Indochina Peninsula (Figure 1a). Four large transboundary rivers pass through the region, namely the Irrawaddy River, the Salween River, the Mekong River, and the Red River. The GMS is dominated by monsoon climates, with the rainy season of approximately half a year (from May to October) and the dry season of another half year (from November to April of the next year) in most areas. The precipitation in the wet season accounts for more than 80% of the total annual precipitation. It is affected by the East Asian and Indian summer monsoon [50]. The GMS is vulnerable to hydrological extremes such as floods or droughts [51]. Due to a large area of arable land (Figure 1c), grain yield is high in the GMS, which plays a critical role in food safety and human livelihoods; furthermore, agriculture is the major contributor to the local economy.

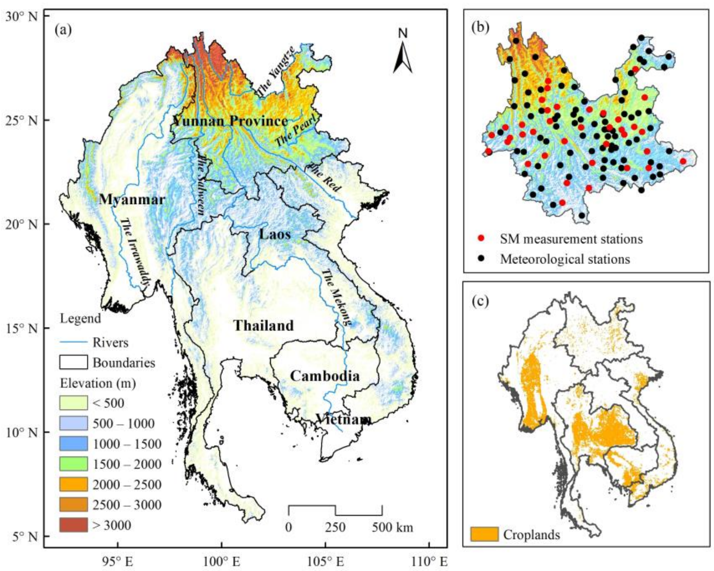

Figure 1. Study area (**a**), location of stations (**b**), and spatial distribution of croplands (**c**).

2.2. Materials

2.2.1. ESACCI SM

The ESACCI SM dataset merges multiple SM products derived from 10 microwave remote sensing sensors. It comprises three products: the ACTIVE, the PASSIVE, and the COMBINED, combining the advantages of these sensors. All three products are representative of the first few centimeters of soil (0–5 cm) [18,24]. In this study, the ESACCI

COMBINED product of version 6.1, which covers 20 years of SM data from January 2001 to December 2020, was used (Table 1).

Table 1. List of data used in this study.

Index	Datasets	Resolution	Source
Surface SM	ESACCI	0.25°, daily	https://www.esa-soilmoisture-cci.org/, accessed on 9 October 2021
Surface SM	In situ	Point, hourly	Yunnan Meteorological Service
Surface albedo	MOD09A1	500 m, 8-day	https://search.earthdata.nasa.gov/, accessed on 9 October 2021
LST	MOD11A2	1 km, 8-day	https://search.earthdata.nasa.gov/, accessed on 9 October 2021
NDVI	MOD13A3	1 km, monthly	https://search.earthdata.nasa.gov/, accessed on 9 October 2021
Land cover type	MCD12Q1	500 m, yearly	https://search.earthdata.nasa.gov/, accessed on 9 October 2021
Precipitation	CHIRPS	0.05°, monthly	https://data.chc.ucsb.edu/products/, accessed on 22 January 2021
Elevation	SRTM	90 m, –	https://srtm.csi.cgiar.org/, accessed on 11 September 2021
Percent of clay, sand, and silt	HWSD	30″, –	https://www.fao.org/soilsportal/, accessed on 9 October 2021
Precipitation, temperature, relative humidity, wind speed, and sunshine duration	Meteorological data	Point, daily	Yunnan Meteorological Service

2.2.2. Auxiliary Data

The auxiliary data used in SM data reconstruction include precipitation, surface albedo, land surface temperature (LST), normalized difference vegetation index (NDVI), soil texture, and elevation (Table 1). Monthly precipitation data were collected from the Climate Hazards Group Infrared Precipitation with Stations (CHIRPS) [52]. The surface albedo, LST, and NDVI were from Moderate-Resolution Imaging Spectroradiometer (MODIS) products: MOD09A1, MOD11A1, and MOD13A2. The surface albedo was calculated using different bands of MOD09A1 product [53]. Before using MODIS products, their outliers were first eliminated according to the quality control file. Then, the eliminated values were supplemented using the Savitzky–Golay (S-G) filter [54] and the Inverse Distance Weight (IDW) method [55]. The elevation and soil texture data were collected from Shuttle Radar Topography Mission (SRTM) [56] and Harmonized World Soil Database (HWSD) [57], respectively. In addition, the yearly land cover product (MCD12Q1) [58] was also applied to explore the influence of agricultural drought on cropland in the GMS.

2.2.3. Ground-Based Observation Data

In situ, SM data from 37 automatic measurement stations during 2016–2020 were collected, with a topsoil depth of 0–10 cm and a temporal resolution of an hour over Yunnan Province in China. To unify all products, the temporal resolution of ground-observation SM data was resampled into a monthly average. In addition, daily precipitation, temperature, relative humidity, wind speed, and sunshine duration during 2001–2020 were obtained from 122 meteorological stations in Yunnan Province. The in situ SM and meteorological data were acquired from the Yunnan Meteorological Service, which had been quality controlled. The locations of automatic measurement stations and meteorological stations are shown in Figure 1b.

2.3. Methods

As shown in Figure 2, the framework of this study includes four parts—part 1: data preparation; part 2: calculation of SSMI using high spatial resolution SM data; part 3:

identification of agricultural droughts based on a 3D method and part 4: calculation of cropland's exposure to agricultural drought events.

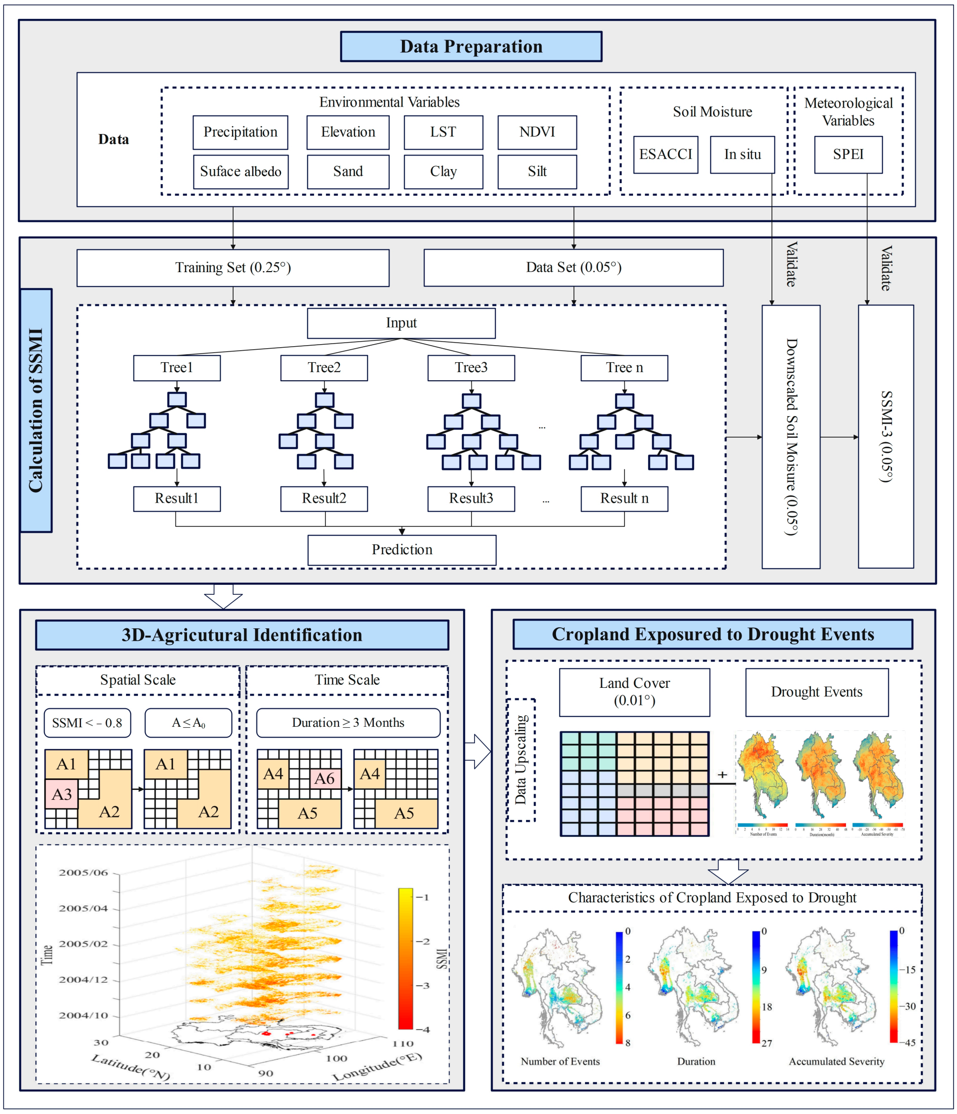

Figure 2. Methodological framework of this study.

2.3.1. Data Processing

Because of the different spatial and temporal resolutions of the data used in this study, we established a uniform data preprocessing standard. All grid data used in SM data reconstruction were reprojected to GCS-WGS-1984 coordinates, and the spatial resolution was resampled to 0.25° and 0.05°. Time series data, including SM, precipitation, NDVI, LST, and surface albedo, were converted to monthly averages. For comparison purposes, these datasets used a common recording period (January 2001–December 2020). In addition, the units of in situ SM data were converted to volume water content (m^3/m^3), consistent with the ESACCI SM units.

2.3.2. Calculation of SSMI and SPEI

The ESACCI SM dataset has many missing or poor-quality pixels and relatively coarse spatial resolution. Therefore, we implemented an SM data reconstruction framework using an ML method to obtain high spatial resolution (0.05°) SM data in the GMS. As a classic ML method, the RF model proposed in 2001 uses multiple decision trees to formulate an ensemble learning algorithm [59]. It has been widely used in various data predictions and reconstructions because of its excellent learning and predicting ability [60,61]. The specific structure of the model is described in previous studies [59,60,62]. In this study, the precipitation, LST, NDVI, surface albedo, elevation, and soil texture were chosen as input environmental variables in the reconstruction process because they can explain the SM variation. First, we set the RF model to establish a nonlinear relationship between the input environmental variables and the available ESACCI SM dataset at the coarser spatial resolution (0.25°). In this process, 70% of the total number of samples were randomly selected as a training set, and the remaining 30% were selected as a validation set for the training process [63,64]. The settings of the parameters in the RF model are shown in Table S1. Second, environmental variables with a fine spatial resolution (0.05°) were introduced to the trained RF model to obtain high-resolution reconstructed SM data. Finally, the reconstructed SM data were validated with the in situ SM data.

The SSMI was applied to identify agricultural drought events using the reconstructed SM data for 2001–2020. The calculation method of the SSMI used the following formula:

$$SSMI_{i,j} = \frac{SM_{i,j} - \bar{SM}_j}{\sigma_j} \tag{1}$$

where i represents the ith year from 2001 to 2020, j represents the jth month, and SM_j and σ_j are the mean and standard deviation values, respectively, in the jth month. Moreover, $SSMI_{i,j}$ and $SM_{i,j}$ express SSMI and SM of the ith year and jth month, respectively [65].

In this research, we chose the 3-month scale SSMI (SSMI-3) to identify agricultural drought events for its effective application in various long-term regional or global drought assessments [66,67]. According to the agricultural drought classifications based on SSMI, SSMI-3 less than −0.8 was identified as drought [8].

The SPEI has been used in an increasing number of drought studies. It combines the variability of precipitation and temperature and has the characteristics of dimensionless, standardized, and multi-time scales [68]. Generally, a 3-month-timescale SPEI (SPEI-3) is suitable for describing agricultural drought. Therefore, in this study, SPEI-3 was calculated based on precipitation, temperature, relative humidity, wind speed and sunshine duration data collected from 122 meteorological stations during 2001–2020 to validate the SSMI-3. The specific description of the SPEI calculation method is shown in Text S1 in the Supplementary. There were four evaluation indicators for the validation assessment, namely the Pearson correlation coefficient (R), root mean square error (RMSE), unbiased root mean square error (ubRMSE), and Bias, the details of which were presented in the earlier publications [64].

2.3.3. Drought Events Identification Based on a 3D Method

A 3D method was used to extract spatiotemporal continuous drought events based on the SSMI. The drought event identification included two steps: (1) Identification of drought patches: The grids with SSMI-3 less than −0.8 were determined as drought patches and were spatially adjacent. In this process, the area of the drought patch (A) smaller than a threshold (A_0, 1.5% of the study area) was ignored [69]. (2) Temporal connections of drought patches: After identifying the drought patches of each month, it was necessary to judge whether they were continuous in time. The overlapping area of drought patches for two neighboring months was used to determine whether the patches were continuous in time. Only the overlapping area that exceeded the threshold (A_0) was defined as the same drought event. In this study, drought events lasting at least three consecutive months were retained for further study.

The drought features extracted based on the 3D identification method could comprehensively reflect the spatiotemporal continuous evolution characteristics of drought. In this study, four drought characteristics were considered: (1) Drought duration (months): It represented the duration of a drought event, which could also be considered the height of a spatiotemporal continuum of drought events. (2) Drought area (km^2): It expressed the area swept by a drought event. In 3D drought identification, it was also considered a vertical projected area of the spatiotemporal continuum of drought events on the two-dimensional (2D) geographic coordinate plane. (3) Drought severity (month·km^2): It represents the degree of water shortage in arid areas and is calculated by a cumulative value of the SSMI-3 over total grid pixels within the 3-D space-time domain. (4) Drought center: The location of the centroid of a 2D layer or 3D volume represented the event's center.

2.3.4. Cropland's Exposure to Agricultural Droughts

Exposures are defined as social, economic, or cultural assets that might be adversely affected by location and environmental impacts [70]. Therefore, to reflect the spatial differences of cropland exposed to drought and the comprehensive impact of drought on the cropland, we need to evaluate cropland exposure during the research period. In this study, the spatial location of drought characteristics over the years—the area, duration, and drought severity—was superimposed on the spatial distribution of cropland from land cover data to explore the effects of drought on cropland and the spatiotemporal distribution of drought-affected cropland.

3. Results

3.1. SM Data Reconstruction and Validation

Figure 3 shows the performance of the RF model at coarse resolution. As shown, the validation subsets had satisfactory results in terms of *R*, RMSE, and Bias metrics. These results suggest that the RF model could generalize data beyond the training sets. Specifically, the validation subset achieved high *R* (approximately 0.82) and small RMSE (approximately 0.04 m^3/m^3) and Bias values (close to 0 m^3/m^3). Most of the reconstructed values were around the 1:1 fitted line, indicating that the RF model could fit the relationships between the environmental variables and the ESACCI SM dataset well at the coarser resolution. Subsequently, high-resolution environmental variable data (0.05°) were input to the trained model to obtain high-resolution SM data from January 2001 to December 2020. Figures 4 and 5 show the spatial pattern of the original ESACCI and reconstructed SM data from January 2004 to December 2006, respectively. The original ESACCI SM dataset had large areas with invalid values because of radio frequency interference, dense vegetation, and satellite operation gaps [71]. The wide distribution of invalid values and the coarse spatial resolution limited their ability to estimate SM. In contrast, the reconstructed SM data not only improved the ability to express details but also achieved spatial full coverage. Moreover, the variations between dry and wet seasons could be well reflected by the reconstructed SM data, indicating that the reconstructed SM data could reveal SM dynamics.

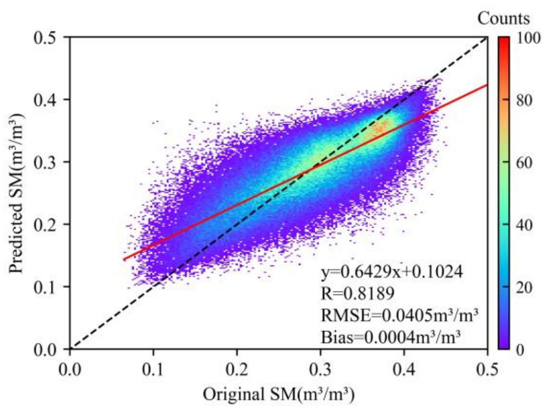

Figure 3. Scatter plot of the predicted values based on RF of the validation set.

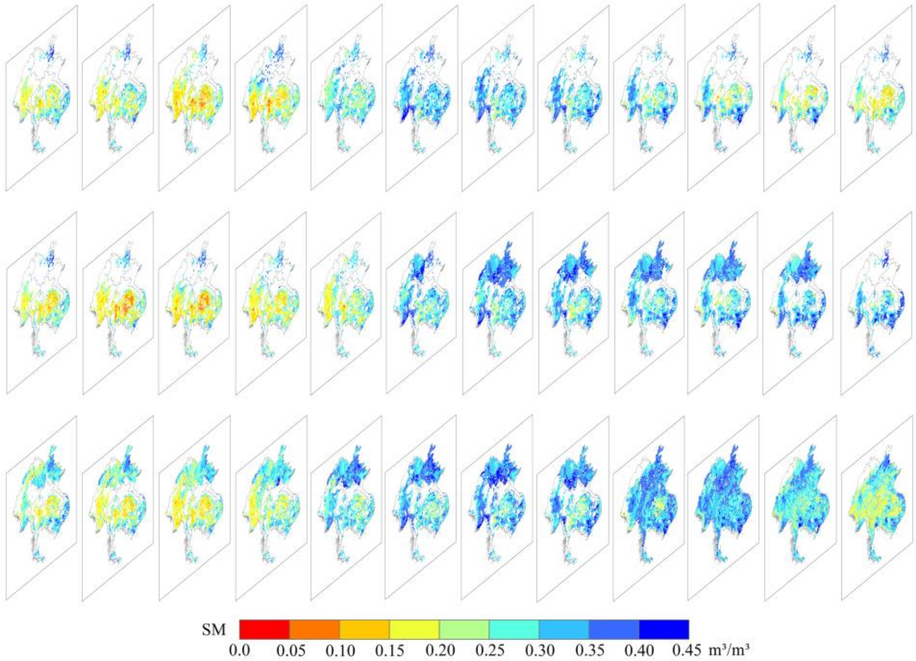

Figure 4. Spatial distribution of ESACCI monthly SM from January 2004 to December 2006.

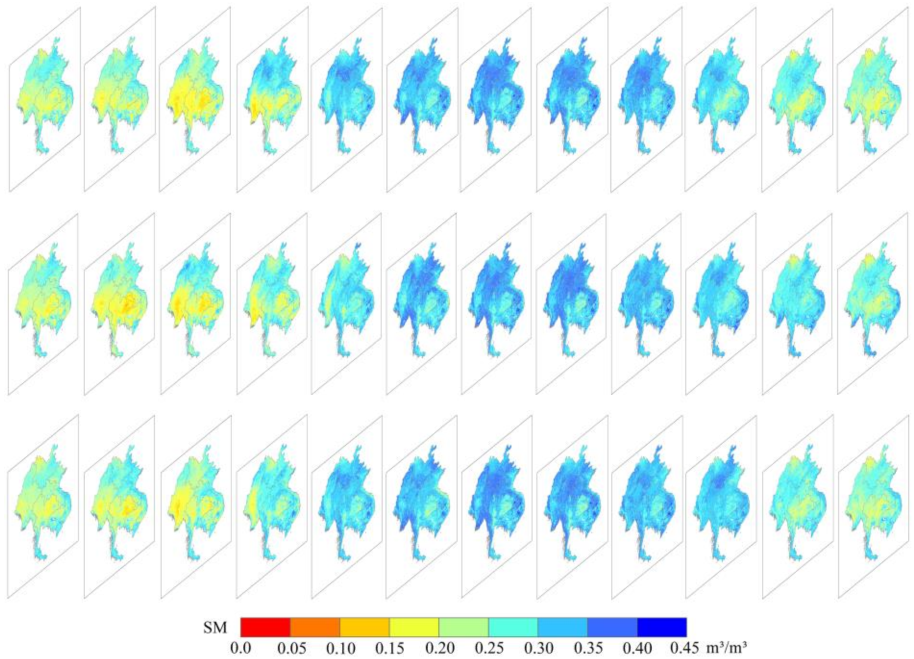

Figure 5. Spatial distribution of reconstructed monthly SM from January 2004 to December 2006.

The reconstructed SM data with 0.05° resolution were validated using the in situ SM from 37 site observations over the Yunnan Province from January 2016 to December 2020. Figure 6 displays the spatial distributions of the *R*, ubRMSE, and Bias values at every site. The consequences revealed that approximately 65% of the observations had *R* values higher than 0.60, approximately 50% of the observations had ubRMSE values below 0.04 m^3/m^3, and over 80% of the observations had absolute Bias values below 0.1 m^3/m^3. Generally, the reconstructed SM data had relatively good accuracy at most sites except for some sporadic sites in mountainous areas or valleys. Usually, the reliability of microwave SM data is relatively low in areas with complex terrain. Moreover, a satellite-based environmental variable usually marked as low quality would be discarded, which may reduce the accuracy of the RF algorithm to estimate SM in these areas during the training process [13]. In addition, it should be noted that the verification consequences would be affected by the limited number of observations, the difference in the spatial scale of observation networks and the reconstructed SM data, and the different surface soil depths of different SM products [64,72]. Nevertheless, the validation results of the reconstructed SM data had the median values for ubRMSE, Bias, and R of 0.0406 m^3/m^3, −0.0294 m^3/m^3, and 0.7197, respectively, indicating that the reconstructed SM data were agreed well with the in situ SM data.

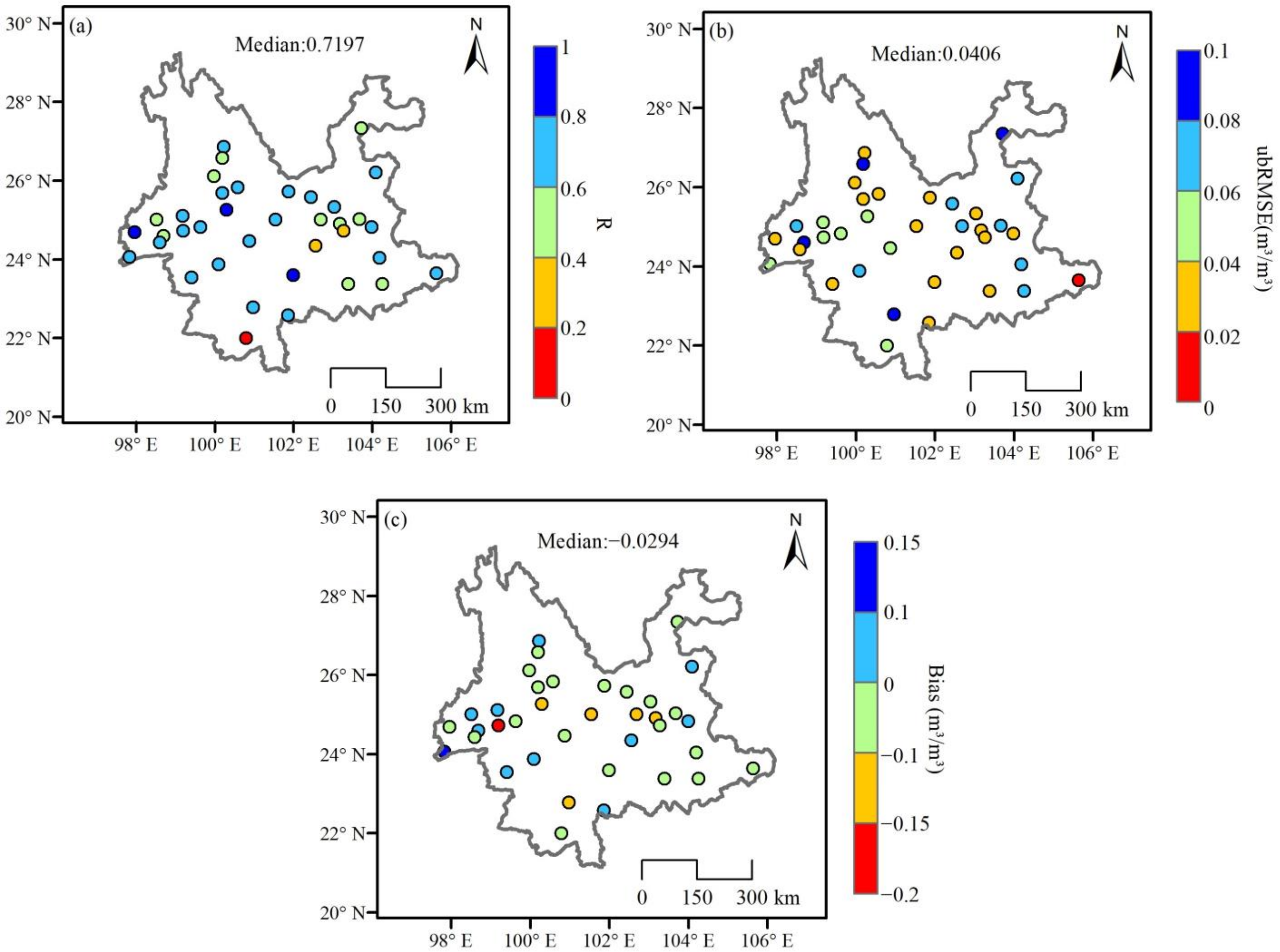

Figure 6. Validation results of the reconstructed SM data using in situ observations: (**a**) R, (**b**) ubRMSE, and (**c**) Bias.

3.2. Agricultural Drought Identification Based on 3D Method

Based on the reconstructed SM data, the SSMI-3 was calculated in the GMS over the 2001–2020 period. Usually, drought indices according to remote sensing need to be verified by indices according to in situ observations to prove their reliability [7]. In agricultural drought monitoring, the SPEI can be used as a benchmark to verify the reliability of SSMI [8]. In addition, good agreement was found between SSMI and SPEI over the GMS [73]. Thus, to verify the SSMI reliability, the accordance between the two indices was analyzed by evaluation of the linear correlation. Figure 7 illustrates the spatial distribution of R between SSMI-3 and SPEI-3 during 2001–2020. It was found that the SSMI-3 significantly correlates with the SPEI-3, varying between 0.12 and 0.77, with a median R-value of 0.5851. At more than 95% of the sites, the correlation between SSMI-3 and SPEI-3 was significant (p < 0.05), which proved that the reliability of the SSMI based on the reconstructed SM data could identify agricultural drought.

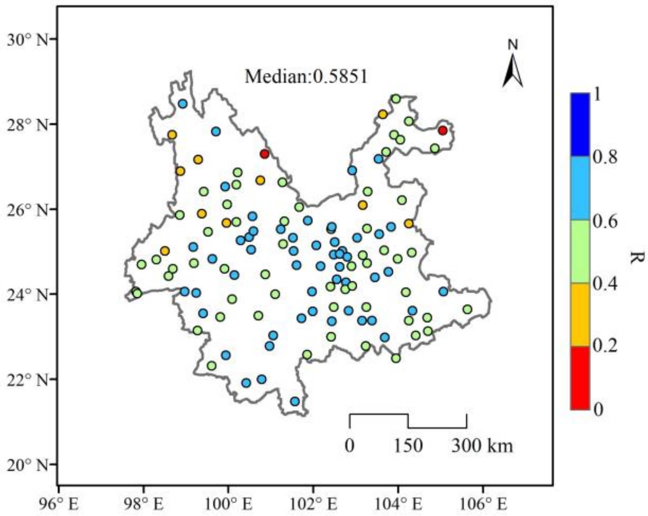

Figure 7. *R* between SSMI-3 and SPEI-3 during 2001–2020.

Based on the SSMI-3, a total of 20 drought events were identified during 2001–2020 over the GMS by the 3D identification method. Table 2 demonstrates the drought characteristics of each agricultural drought event. It could be seen that the drought durations varied from 3 months to 23 months, with an average value of 7 months. The drought areas ranged from 1.95×10^5 km^2 to 23.24×10^5 km^2 with an average value of 9×10^5 km^2. Drought severity ranged from -4.62×10^5·month·km^2 to -207.44×10^5·month·km^2, with an average value of approximately -45.6×10^5 month·km^2. Within the two decadal categories (2001–2010 and 2011–2020), the number of droughts, duration, and absolute values of drought events' severity for the periods of 2011–2020 increased by 22.22%, 65.38%, and 32.75%, respectively, compared with the periods of 2001–2010. Concerning the drought timing, most of the drought events started in autumn (45% of the total droughts), followed by spring, winter, and summer. Additionally, most drought events ended in summer or spring (70% of total droughts).

Table 2. Drought characteristics of agricultural drought events from 2001 to 2020.

Drought Event Number	Duration (Months)	Beginning Time (Year/Month)	Ending Time (Year/Month)	Drought Center			Drought Area (10^5 km^2)	Drought Severity (10^5·Month·km^2)
				Time (Year/Month)	Longitude (°E)	Latitude (°N)		
1	3	2001/03	2001/05	2001/04	97.69	23.68	5.87	−10.05
2	3	2002/04	2002/06	2002/05	99.79	19.10	2.67	−4.62
3	3	2002/09	2002/11	2002/10	98.60	23.28	1.95	−5.01
4	10	2003/07	2004/04	2003/11	100.14	19.61	15.95	−66.74
5	9	2004/10	2005/06	2005/02	102.09	16.57	19.40	−118.60
6	3	2005/05	2005/07	2005/06	99.15	23.63	6.95	−16.22
7	5	2006/11	2007/03	2007/01	102.22	18.02	9.28	−24.51
8	4	2009/01	2009/04	2009/02	100.19	22.25	8.87	−19.35
9	12	2009/09	2010/08	2010/02	101.25	19.79	21.16	−126.42
10	5	2011/06	2011/10	2011/08	103.41	25.16	2.67	−13.02
11	6	2011/10	2012/03	2011/12	97.92	25.34	4.32	−11.45
12	4	2012/03	2012/06	2012/04	101.61	23.97	5.02	−10.34
13	10	2012/10	2013/07	2013/02	99.88	21.44	15.54	−57.32
14	3	2012/11	2013/01	2012/12	105.59	14.74	2.60	−5.17
15	3	2014/02	2014/04	2014/03	100.62	12.46	2.10	−4.74
16	6	2014/02	2014/07	2014/04	100.19	22.82	10.16	−30.83
17	6	2014/09	2015/02	2014/11	96.58	22.94	5.40	−20.64
18	17	2015/04	2016/08	2015/12	102.62	16.40	20.97	−150.72
19	3	2018/10	2018/12	2018/11	105.76	15.04	2.74	−8.08
20	23	2019/01	2020/11	2019/12	100.64	18.54	23.24	−207.44

Severity denotes the accumulated water shortfall over the entire drought duration and areal extent during a drought event, which is a composite parameter affected by both drought area and drought duration. Thus, we selected the severest drought event during 2019–2020 as an exemplary drought event and illustrated its evolution process. The evolution process of the drought event and its characteristics are shown in Figure 8. In the first month of the event, which started in January 2019 in northern Cambodia, the total area of the drought patch was approximately 0. 48 $\times$ 10^5 km^2, accounting for 1.88% of the total area (Figure 8a,b). The expansion of arid space developed slowly in the first 3 months. From March 2019, the drought area expansion developed rapidly and reached its first peak by May 2019, with the drought area approximately 13.31 $\times$ 10^5 km^2, accounting for 51.93% of the total area. The total area had been shrinking over the next 3 months. In the following 11 months, the overall trend of the drought area showed a slow expansion until July 2020, when the dry area reached its second peak of 11.93 $\times$ 10^5 km^2. After that, the drought area began to shrink again until the event ended in November 2020. The patterns of variation in severity were analogous to that in the area: two peaks of drought severity were reached at approximately -22.19×10^5 month·km^2 and -19.55×10^5 month·km^2 in May 2019 and July 2020, respectively (Figure 8b).

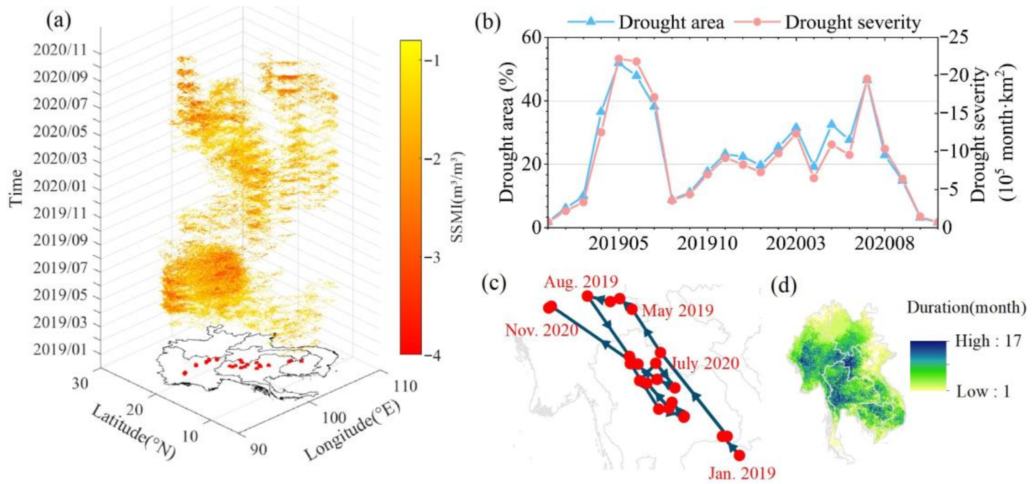

Figure 8. Three-dimensional identification results of the most severe drought from January 2019: (**a**) three-dimensional drought event; (**b**) temporal evolution of area and severity; (**c**) centers routine of the drought event; (**d**) spatial distribution of duration.

The drought event had a long centroid movement from the southeast to the northwest of the GMS (Figure 8c). The drought first occurred concentratedly in northern Cambodia in January 2019, and then the drought center gradually moved to the northwest. The center of the drought patch extended to eastern Myanmar with an average speed of 287.27 km per month when the drought reached its severest month (May 2019)—its first drought peak. Afterward, drought severity began to moderate until, in August 2019, it reached a local minimum. However, after that, the drought severity gradually increased with the drought centroids moving northeastward and gathering in Thailand. When it reached its second peak (July 2020), the center was still located in Thailand. After that, the drought slowed; its centroids moved northwest again and finally ended in north-central Myanmar in November 2020. This 23-month drought event affected approximately 90% of the study area. The centroid's movement had a total length of 4030 km. Central and western Myanmar, the border between Laos and Myanmar, central and western Thailand, and central and northern Cambodia experienced a long drought, with a duration of more than 8 months (Figure 8d).

Figure 9 shows the spatial patterns of drought frequency, duration, and accumulated severity of the agricultural drought of each grid over the GMS during 2001–2020. Approximately 16% of the total area experienced more than 10 events during the two decades. These areas were mainly located in the western Yunnan Province and northeastern Myanmar (Figure 9a). Approximately 5% of the total area experienced more than 35 months of drought during the 20 years, meaning these regions had experienced drought at least 15% of the time in the past 20 years (Figure 9b). These regions were mainly located in the southern Yunnan Province, middle and eastern Myanmar, and northern Thailand and Laos. The drought severity presented a similar spatial pattern to the duration (Figure 9c). The area with a larger duration and severity indicated a relatively high level of agricultural drought risk.

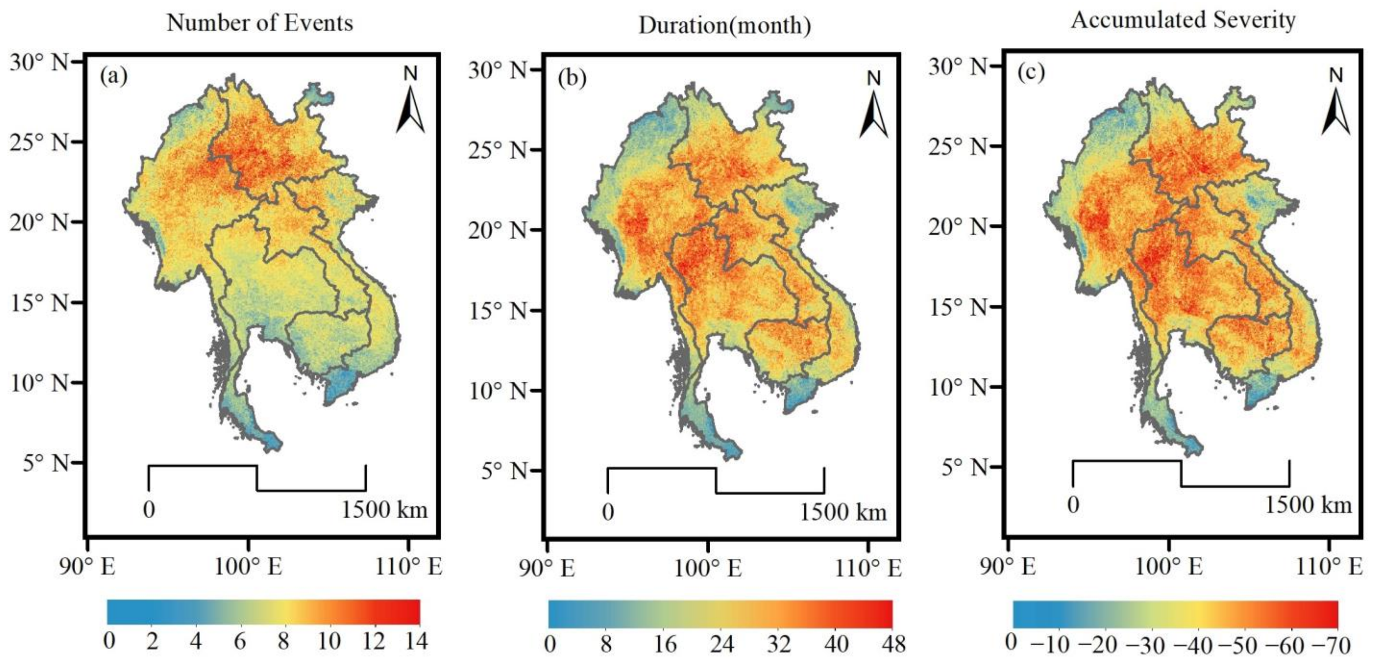

Figure 9. Spatial patterns of different drought characteristics: (**a**) number of events, (**b**) duration, and (**c**) accumulated severity.

3.3. Cropland's Exposure to Drought Events

To analyze the cropland's exposure to agricultural drought events, the cropland in the MODIS land cover data was extracted from 2001 to 2020, as shown in Figure 10. During 2001–2020, the average cropland was 4.97 $\times$ 10^5 km^2 over the GMS. Spatially, large areas of continuous cropland were distributed in central and southern Myanmar, central and southern Thailand, and the Tonle Sap Lake floodplain in Cambodia. In contrast, Yunnan Province, Vietnam, and Laos had a sporadic cropland distribution with a relatively small area. Since the cropland area had remained stable over the past two decades, the cropland area exposed to drought mainly depended on droughts rather than cropland expansion. Table 3 presents the characteristics of cropland exposed to the identified agricultural droughts. The data illustrate that the cropland area affected by agricultural droughts ranged from 0.07 to 4.72 $\times$ 10^5 km^2, with an average value of 1.71 $\times$ 10^5 km^2, accounting for 34% of the total cropland over the GMS. As expected, the four severest drought events (Nos. 5, 9, 18, and 20) affected more than 80% of the total cropland area.

Figure 11 shows the spatial distribution of cropland exposed to agricultural drought in different periods. During 2001–2020, cropland exposure was generally high in Myanmar, Thailand, and Cambodia, which had large cropland areas. On the contrary, cropland exposure was low in Laos, Vietnam, and Yunnan Province due to the limited cropland areas (Figure 11a). Spatially, cropland exposed to more, longer, and more severe agricultural drought events was observed in central and southern Myanmar. In Thailand and Cambodia, cropland suffered from less but severer droughts. Compared with 2001–2010, cropland was exposed to agricultural drought with fewer events but higher severity in central Myanmar during 2011–2020 (Figure 11b,c). In addition, the cropland in Yunnan Province and Thailand experienced more and severer agricultural droughts from 2011 to 2020.

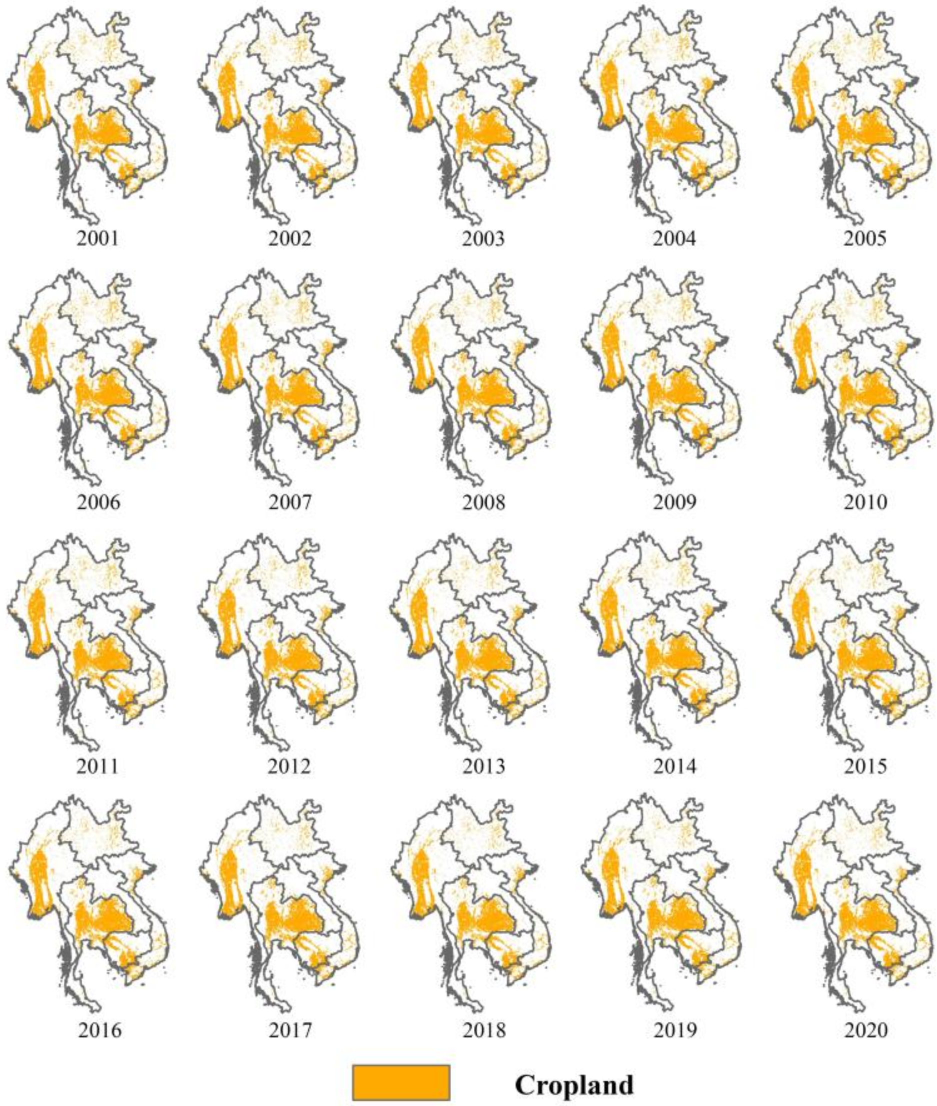

Figure 10. Spatial distribution of cropland from 2001 to 2020.

Table 3. Characteristics of crops exposed to drought.

Drought Event Number	Total Cropland (10^5 km^2)	Cropland Exposed to Drought (10^5 km^2)	Percentage	Drought Event Number	Total Cropland (10^5 km^2)	Cropland Exposed to Drought (10^5 km^2)	Percentage
1	4.85	0.83	17.18	11	4.97	0.25	4.96
2	4.90	0.60	12.29	12	4.97	0.25	5.08
3	4.90	0.07	1.40	13	5.01	3.22	64.19
4	4.96	3.34	67.21	14	4.97	0.94	18.84
5	5.02	4.41	87.95	15	5.04	0.11	2.19
6	5.02	1.05	20.87	16	5.04	0.82	16.21
7	5.00	1.65	33.02	17	5.04	1.13	22.35
8	4.99	1.09	21.91	18	5.06	4.59	90.66
9	5.01	4.43	88.52	19	4.85	0.58	11.89
10	4.97	0.19	3.80	20	4.85	4.72	97.30

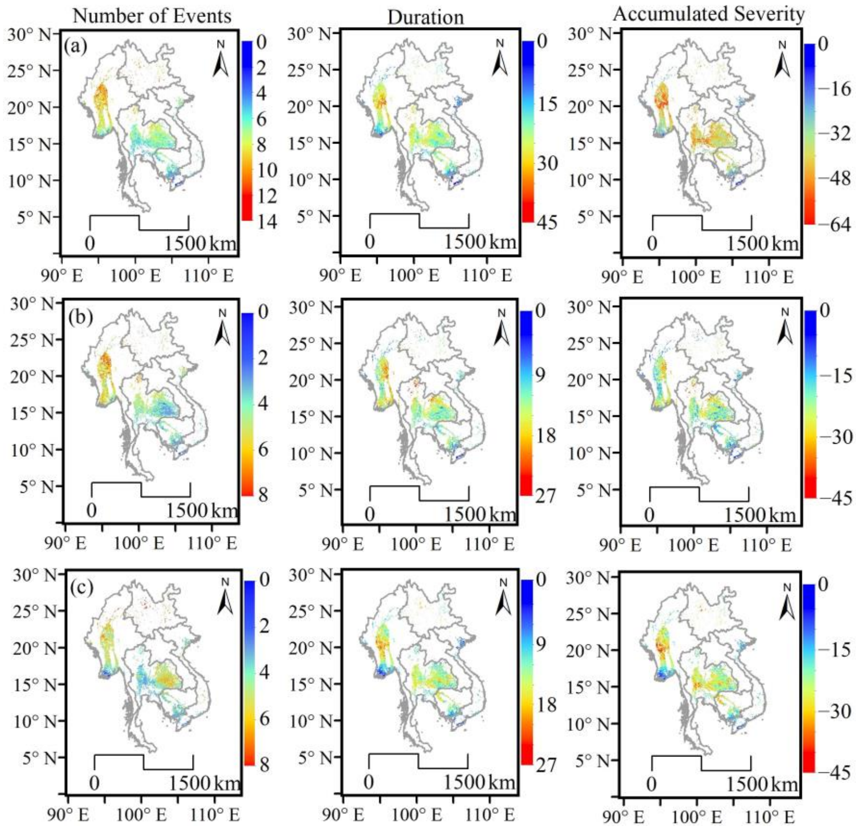

Figure 11. Spatial distribution of cropland exposed to agricultural drought in different periods. (**a**) 2001–2020, (**b**) 2001–2010, and (**c**) 2011–2020.

4. Discussion

SM is considered a key indicator for representing agricultural drought. However, obtaining the in situ SM data over the GMS is difficult due to the scarcity of monitoring networks [74]. Although the ESACCI SM dataset has broad application prospects in agricultural drought monitoring, the applications are co-limited by missing data and coarse spatial resolution. In this study, we proposed an SM data reconstruction approach combining the ESACCI SM dataset, environmental variables, and the RF model to obtain high spatial resolution SM data over the GMS. The results showed that the reconstructed SM data achieved spatial continuity and improved spatial resolution. The validation based on 37 in situ SM data points indicated that the reconstructed SM data agreed well with the in situ data, with median values for ubRMSE, Bias, and *R* of 0.0406 m^3/m^3, -0.0294 m^3/m^3, and 0.7197, respectively. Compared with the verification results of the original ESACCI SM dataset in China [21] and Yunnan Province [75], the reconstructed SM data in this study achieved even better comparable performance. Although the verified sites are limited and distributed in Yunnan Province, we are confident that the reconstructed SM data will perform better in other regions. This is because Yunnan is a region with complex terrain and low-quality remotely sensed SM and environmental variables data, inevitably affecting the SM data reconstruction process. However, the correlations between remotely sensed SM and environmental variables are expected to be higher in flat areas [13].

ML was widely used in many SM reconstruction studies because it could well fit and establish the nonlinear relationship between various environmental variables and SM data [71,76]. In this study, the SM data reconstruction achieved satisfactory results using the RF model due to its outstanding performance in fitting data. However, the RF algorithm is unable to consider the spatiotemporal neighborhood relationships. Deep learning can extract the temporal and spatial features of continuous spatiotemporal data [77,78]. Thus, the use of deep learning may provide better results [31,79]. In the process of SM data reconstruction, analyzing the importance of these environmental variables would help to understand the mechanism of their impact on SM [30]. Figure S1 shows the averaged variable importance scores for environmental variables. It was proven that precipitation played the most important role because it was a key variable that directly caused changes in surface SM [30]. Local topography had a greater impact on SM changes in areas with large elevation fluctuations, and LST controlled the energy exchange at the land surface. Therefore, elevation and LST also had high importance in the reconstruction process, consistent with the other studies [64,80]. In addition, NDVI and surface albedo were also relatively important in SM data reconstruction because they could reflect vegetation conditions and surface energy exchange, respectively [64].

Traditional drought event identification only describes drought from a time or space perspective and cannot describe drought's change process from the perspective of temporal and spatial continuity [32,69]. In this study, we presented a 3D method to identify agricultural drought events using reconstructed high spatial resolution SM data. There were 20 droughts identified lasting at least 3 months, which meant the GMS suffered from drought on average once per year. As expected, notoriously severe droughts were ranked high in the consequences, such as the 2019–2020 event [81], the 2015–2016 event [82], the 2009–2010 event [48], and the 2004–2005 event [45], which indicated that the 3D method was to be reliable for drought events detection. Furthermore, the relationship among the severity, area, and duration of drought events was explored, as shown in Figure S2. The drought severity showed exponential and linear changes with drought area and duration. The fitted exponential and linear functions had R^2 of 0.99 and 0.92, respectively. Meanwhile, the log function was used to fit the area and duration, with an R^2 of 0.84. Similarly, another drought analysis using a 3D algorithm also indicated that the drought severity significantly correlated with drought area and duration [37,83], which would help to analyze drought frequency and assess drought impacts.

There are noticeable disparities in the spatiotemporal changes of agricultural droughts because of the diversity in climate, topographical reliefs, and geography of the GMS. For example, the Rakhine Yoma mountain range cast a rain shadow over a large portion of central Myanmar, which as a result receives less precipitation and is more likely to experience droughts [84]. Thailand regularly experiences yearly droughts because of an increase in average annual temperature and a decrease in mean annual rainfall [85]. It is found that cropland exposure is high in Myanmar, Thailand, and Cambodia, where there is a large area of cropland. On average, the cropland exposure over the GMS was 1.71×10^5 km^2, which accounted for 34% of the total cropland. Notably, the four severest drought events affected more than 80% of the total cropland area. Irrigation is an effective measure to resist drought. However, the majority of the agriculture in the GMS is rain-fed. Figure S3 shows different irrigation levels over cropland in the GMS. The irrigation data were collected from global irrigation data during 2001–2015 [86]. Approximately 18% of the total cropland achieved high irrigation, mainly distributed in Vietnam's Mekong and Red Delta, Chao Phraya River basin in Thailand, and Irrawaddy Delta in Myanmar. However, approximately 82% of the total cropland had low or no irrigation, which is common in whole regions. This situation made the cropland vulnerable to agricultural drought. The rice production and export volume of GMS regions rank among the top in the world [87], and rain-fed rice cultivation means food security [88]. To deal with the increasing drought events in the future [89], some successful experiences to learn from include: (1) effective risk management measures by governments and cross-regional cooperation, such as the Lancang-Mekong Cooperation mechanism; (2) strengthening infrastructure investment and (3) improving drought early warning and real-time monitoring means [90].

5. Conclusions

In this research, we proposed an integrated approach for detecting agricultural droughts and their cropland exposure using remote sensing data over the GMS. The SM dataset (0.05°) was first reconstructed using an RF model based on the ESACCI SM dataset. The validation results indicated that the reconstructed SM data achieved satisfactory results and could be confidently applied in agricultural drought monitoring. The SM data reconstruction filled the gap in using satellite SM data for drought monitoring, co-limited by missing data and coarse spatial resolution. Furthermore, 3D drought identification results provided more comprehensive insights into the spatiotemporal continuous evolution process of agricultural droughts. In essence, the GMS has faced severe agricultural droughts in the last two decades, highlighting the worth of comprehensive impact assessments of agricultural droughts. It was found that cropland exposure was high in Myanmar, Thailand, and Cambodia. Severe droughts coupled with insufficient irrigation in the Mekong countries require timely preparation and adaptation to strengthen agricultural resilience to climate change. The integrated approach proposed in this research can be extended to other vegetated regions with limited in situ data available to provide detailed spatiotemporal characteristics of agricultural droughts. Moving forward, the capability of this approach in drought monitoring can be further improved by using more advanced deep-learning models and finer remote sensing data.

Supplementary Materials: The following supporting information can be downloaded at: https://www.mdpi.com/article/10.3390/rs15112737/s1, Table S1: Parameter settings in RF model; Figure S1. The importance scores for environmental variables; Figure S2. Relationships between drought characteristics: (a) severity and area; (b) severity and duration and (c) area and duration; Figure S3. Irrigation levels over cropland in the GMS from 2001 to 2015; Text S1: The calculation method of SPEI index.

Author Contributions: Conceptualization, W.M. and Y.L. (Yungang Li); methodology, W.M., Y.L. (Yungang Li) and Y.L. (Yunshu Long); software, X.L. (Xuan Luo) and Y.L. (Yunshu Long); validation, X.J.; formal analysis, W.M.; investigation, X.L. (Xuan Luo), Y.L.(Yunshu Long) and X.X.; resources, X.J.; data curation, X.X.; writing—original draft preparation, W.M.; writing—review and editing, Y.L. (Yungang Li); visualization, X.L. (Xian Luo); supervision, X.L. (Xian Luo); project administration, Y.L. (Yungang Li); funding acquisition, Y.L. (Yungang Li). All authors have read and agreed to the published version of the manuscript.

Funding: This work was funded by the National Key Research and Development Program of China (Grant No. 2022YFF1302405, Yungang Li), the National Natural Science Foundation of China (Grant No. 42067033, Yungang Li), and Applied Basic Research Programs of Yunnan Province (Grant No. 202001BB050073 and Grant No. 202101AT070075, Yungang Li).

Data Availability Statement: The ESACCI product can be obtained at https://www.esa-soilmoiture-cci.org/, accessed on 9 October 2021. MODIS data can be accessed at https://search.earthdata.nasa.gov/, accessed on 9 October 2021. CHIRPS precipitation data is available at https://data.chc.ucsb.edu/products/, accessed on 22 January 2021. SRTM can be obtained at https://srtm.csi.cgiar.org/, accessed on 11 September 2021. HWSD can be obtained at https://www.fao.org/soilsportal/, accessed on 9 October 2021.

Acknowledgments: The authors would like to thank the reviewers and the handling editor whose comments and suggestions improved this paper.

Conflicts of Interest: The authors declare no conflict of interest.

References

1. Kang, H.Y.W.; Sridhar, V.; Ali, S.A. Climate change impacts on conventional and flash droughts in the Mekong River Basin. *Sci. Total Environ.* **2022**, *838*, 23. [CrossRef] [PubMed]
2. Zhang, X.; Hao, Z.C.; Singh, V.P.; Zhang, Y.; Feng, S.F.; Xu, Y.; Hao, F.H. Drought propagation under global warming: Characteristics, approaches, processes, and controlling factors. *Sci. Total Environ.* **2022**, *838*, 19. [CrossRef] [PubMed]
3. Vicente-Serrano, S.M.; Quiring, S.M.; Pena-Gallardo, M.; Yuan, S.S.; Dominguez-Castro, F. A review of environmental droughts: Increased risk under global warming? *Earth-Sci. Rev.* **2020**, *201*, 23. [CrossRef]
4. Mishra, A.K.; Singh, V.P. A review of drought concepts. *J. Hydrol.* **2010**, *391*, 204–216. [CrossRef]
5. Carrao, H.; Russo, S.; Sepulcre-Canto, G.; Barbosa, P. An empirical standardized soil moisture index for agricultural drought assessment from remotely sensed data. *Int. J. Appl. Earth Obs. Geoinf.* **2016**, *48*, 74–84. [CrossRef]

6. Mao, Y.; Wu, Z.Y.; He, H.; Lu, G.H.; Xu, H.T.; Lin, Q.X. Spatio-temporal analysis of drought in a typical plain region based on the soil moisture anomaly percentage index. *Sci. Total Environ.* **2017**, *576*, 752–765. [CrossRef]
7. Feng, P.Y.; Wang, B.; Liu, D.L.; Yu, Q. Machine learning-based integration of remotely-sensed drought factors can improve the estimation of agricultural drought in South-Eastern Australia. *Agric. Syst.* **2019**, *173*, 303–316. [CrossRef]
8. Han, Z.M.; Huang, Q.; Huang, S.Z.; Leng, G.Y.; Bai, Q.J.; Liang, H.; Wang, L.; Zhao, J.; Fang, W. Spatial-temporal dynamics of agricultural drought in the Loess Plateau under a changing environment: Characteristics and potential influencing factors. *Agric. Water Manag.* **2021**, *244*, 12. [CrossRef]
9. Chen, X.G.; Li, Y.; Yao, N.; Liu, D.L.; Javed, T.; Liu, C.C.; Liu, F.G. Impacts of multi-timescale SPEI and SMDI variations on winter wheat yields. *Agric. Syst.* **2020**, *185*, 14. [CrossRef]
10. Crow, W.T.; Berg, A.A.; Cosh, M.H.; Loew, A.; Mohanty, B.P.; Panciera, R.; de Rosnay, P.; Ryu, D.; Walker, J.P. Upscaling Sparse Ground-Based Soil Moisture Observations For The Validation Of Coarse-Resolution Satellite Soil Moisture Products. *Rev. Geophys.* **2012**, *50*, 20. [CrossRef]
11. Modanesi, S.; Massari, C.; Camici, S.; Brocca, L.; Amarnath, G. Do Satellite Surface Soil Moisture Observations Better Retain Information About Crop-Yield Variability in Drought Conditions? *Water Resour. Res.* **2020**, *56*, 19. [CrossRef]
12. Zhao, W.; Sanchez, N.; Lu, H.; Li, A.N. A spatial downscaling approach for the SMAP passive surface soil moisture product using random forest regression. *J. Hydrol.* **2018**, *563*, 1009–1024. [CrossRef]
13. Xu, M.Y.; Yao, N.; Yang, H.X.; Xu, J.; Hu, A.N.; de Goncalves, L.G.G.; Liu, G. Downscaling SMAP soil moisture using a wide & deep learning method over the Continental United States. *J. Hydrol.* **2022**, *609*, 22. [CrossRef]
14. Brocca, L.; Hasenauer, S.; Lacava, T.; Melone, F.; Moramarco, T.; Wagner, W.; Dorigo, W.; Matgen, P.; Martinez-Fernandez, J.; Llorens, P.; et al. Soil moisture estimation through ASCAT and AMSR-E sensors: An intercomparison and validation study across Europe. *Remote Sens. Environ.* **2011**, *115*, 3390–3408. [CrossRef]
15. O'Neill, P.; Entekhabi, D.; Njoku, E.; Kellogg, K. The Nasa Soil Moisture Active Passive (Smap) Mission: Overview. In Proceedings of the 30th IEEE International Geoscience and Remote Sensing Symposium (IGARSS) on Remote Sensing—Global Vision for Local Action, Honolulu, HI, USA, 25–30 June 2010; IEEE: Piscataway, NJ, USA, 2010; pp. 3236–3239.
16. Merlin, O.; Escorihuela, M.J.; Mayoral, M.A.; Hagolle, O.; Al Bitar, A.; Kerr, Y. Self-calibrated evaporation-based disaggregation of SMOS soil moisture: An evaluation study at 3 km and 100 m resolution in Catalunya, Spain. *Remote Sens. Environ.* **2013**, *130*, 25–38. [CrossRef]
17. Bao, Y.S.; Lin, L.B.; Wu, S.Y.; Deng, K.A.K.; Petropoulos, G.P. Surface soil moisture retrievals over partially vegetated areas from the synergy of Sentinel-1 and Landsat 8 data using a modified water-cloud model. *Int. J. Appl. Earth Obs. Geoinf.* **2018**, *72*, 76–85. [CrossRef]
18. Gruber, A.; Scanlon, T.; van der Schalie, R.; Wagner, W.; Dorigo, W. Evolution of the ESA CCI Soil Moisture climate data records and their underlying merging methodology. *Earth Syst. Sci. Data* **2019**, *11*, 717–739. [CrossRef]
19. Dorigo, W.A.; Gruber, A.; De Jeu, R.A.M.; Wagner, W.; Stacke, T.; Loew, A.; Albergel, C.; Brocca, L.; Chung, D.; Parinussa, R.M.; et al. Evaluation of the ESA CCI soil moisture product using ground-based observations. *Remote Sens. Environ.* **2015**, *162*, 380–395. [CrossRef]
20. Ma, S.Y.; Zhang, S.Q.; Wu, Q.X.; Wang, J. Long-term changes in surface soil moisture based on CCI SM in Yunnan Province, Southwestern China. *J. Hydrol.* **2020**, *588*, 12. [CrossRef]
21. Wu, X.T.; Lu, G.H.; Wu, Z.Y.; He, H.; Scanlon, T.; Dorigo, W. Triple Collocation-Based Assessment of Satellite Soil Moisture Products with In Situ Measurements in China: Understanding the Error Sources. *Remote Sens.* **2020**, *12*, 2275. [CrossRef]
22. Liu, Y.W.; Liu, Y.B.; Wang, W. Inter-comparison of satellite-retrieved and Global Land Data Assimilation System-simulated soil moisture datasets for global drought analysis. *Remote Sens. Environ.* **2019**, *220*, 1–18. [CrossRef]
23. Almendra-Martin, L.; Martinez-Fernandez, J.; Piles, M.; Gonzalez-Zamora, A. Comparison of gap-filling techniques applied to the CCI soil moisture database in Southern Europe. *Remote Sens. Environ.* **2021**, *258*, 14. [CrossRef]
24. Dorigo, W.; Wagner, W.; Albergel, C.; Albrecht, F.; Balsamo, G.; Brocca, L.; Chung, D.; Ertl, M.; Forkel, M.; Gruber, A.; et al. ESA CCI Soil Moisture for improved Earth system understanding: State-of-the art and future directions. *Remote Sens. Environ.* **2017**, *203*, 185–215. [CrossRef]
25. Zhang, L.Q.; Liu, Y.; Ren, L.L.; Teuling, A.J.; Zhang, X.X.; Jiang, S.H.; Yang, X.L.; Wei, L.Y.; Zhong, F.; Zheng, L.H. Reconstruction of ESA CCI satellite-derived soil moisture using an artificial neural network technology. *Sci. Total Environ.* **2021**, *782*, 16. [CrossRef]
26. Llamas, R.M.; Guevara, M.; Rorabaugh, D.; Taufer, M.; Vargas, R. Spatial Gap-Filling of ESA CCI Satellite-Derived Soil Moisture Based on Geostatistical Techniques and Multiple Regression. *Remote Sens.* **2020**, *12*, 665. [CrossRef]
27. Zhang, Q.; Yuan, Q.Q.; Li, J.; Wang, Y.; Sun, F.J.; Zhang, L.P. Generating seamless global daily AMSR2 soil moisture (SGD-SM) long-term products for the years 2013–2019. *Earth Syst. Sci. Data* **2021**, *13*, 1385–1401. [CrossRef]
28. Zhao, W.; Wen, F.P.; Song, L.S.; Li, X.J.; Li, A.N. Downscaling Smap Passive Soil Moisture Product With Modis Products Over Mountainous Region. In Proceedings of the IEEE International Geoscience and Remote Sensing Symposium (IGARSS), Yokohama, Japan, 28 July–2 August 2019; IEEE: Piscataway, NJ, USA, 2019; pp. 7006–7009.
29. Abbaszadeh, P.; Moradkhani, H.; Zhan, X.W. Downscaling SMAP Radiometer Soil Moisture Over the CONUS Using an Ensemble Learning Method. *Water Resour. Res.* **2019**, *55*, 324–344. [CrossRef]
30. Long, D.; Bai, L.L.; Yan, L.; Zhang, C.J.; Yang, W.T.; Lei, H.M.; Quan, J.L.; Meng, X.Y.; Shi, C.X. Generation of spatially complete and daily continuous surface soil moisture of high spatial resolution. *Remote Sens. Environ.* **2019**, *233*, 19. [CrossRef]

31. Yulin, S.; Xiaoxiao, M.; Zhou, S. Inter-comparison and integration of different soil moisture downscaling methods over the Qinghai-Tibet Plateau. *J. Hydrol.* **2023**, *617*, 17. [CrossRef]
32. Haslinger, K.; Bloschl, G. Space-Time Patterns of Meteorological Drought Events in the European Greater Alpine Region Over the Past 210 Years. *Water Resour. Res.* **2017**, *53*, 9807–9823. [CrossRef]
33. Lloyd-Hughes, B. A spatio-temporal structure-based approach to drought characterisation. *Int. J. Climatol.* **2012**, *32*, 406–418. [CrossRef]
34. Liu, Y.W.; Liu, Y.B.; Wang, W.; Zhou, H. Propagation of soil moisture droughts in a hotspot region: Spatial pattern and temporal trajectory. *J. Hydrol.* **2021**, *593*, 14. [CrossRef]
35. Andreadis, K.M.; Clark, E.A.; Wood, A.W.; Hamlet, A.F.; Lettenmaier, D.P. Twentieth-century drought in the conterminous United States. *J. Hydrometeorol.* **2005**, *6*, 985–1001. [CrossRef]
36. Herrera-Estrada, J.E.; Satoh, Y.; Sheffield, J. Spatiotemporal dynamics of global drought. *Geophys. Res. Lett.* **2017**, *44*, 2254–2263. [CrossRef]
37. Xu, K.; Yang, D.W.; Yang, H.B.; Li, Z.; Qin, Y.; Shen, Y. Spatio-temporal variation of drought in China during 1961–2012: A climatic perspective. *J. Hydrol.* **2015**, *526*, 253–264. [CrossRef]
38. Zhai, J.Q.; Huang, J.L.; Su, B.D.; Cao, L.G.; Wang, Y.J.; Jiang, T.; Fischer, T. Intensity-area-duration analysis of droughts in China 1960–2013. *Clim. Dyn.* **2017**, *48*, 151–168. [CrossRef]
39. Zhan, W.; Guan, K.Y.; Sheffield, J.; Wood, E.F. Depiction of drought over sub-Saharan Africa using reanalyses precipitation data sets. *J. Geophys. Res. Atmos.* **2016**, *121*, 10555–10574. [CrossRef]
40. Wang, A.Q.; Wang, Y.J.; Su, B.D.; Kundzewicz, Z.W.; Tao, H.; Wen, S.S.; Qin, J.C.; Gong, Y.; Tong, J. Comparison of Changing Population Exposure to Droughts in River Basins of the Tarim and the Indus. *Earth Future* **2020**, *8*, 13. [CrossRef]
41. Jiang, S.; Zhou, J.; Wang, G.J.; Lin, Q.G.; Chen, Z.Y.; Wang, Y.J.; Su, B.D. Cropland Exposed to Drought Is Overestimated without Considering the CO_2 Effect in the Arid Climatic Region of China. *Land* **2022**, *11*, 881. [CrossRef]
42. Miao, L.J.; Zhang, J.; Kattel, G.R.; Liu, R. Increased Exposure of China's Cropland to Droughts under 1.5 degrees C and 2 degrees C Global Warming. *Atmosphere* **2022**, *13*, 1035. [CrossRef]
43. Abhishek, A.; Das, N.N.; Ines, A.V.M.; Andreadis, K.M.; Jayasinghe, S.; Granger, S.; Ellenburg, W.L.; Dutta, R.; Quyen, N.H.; Markert, A.M.; et al. Evaluating the impacts of drought on rice productivity over Cambodia in the Lower Mekong Basin. *J. Hydrol.* **2021**, *599*, 13. [CrossRef]
44. Kang, H.; Sridhar, V.; Mainuddin, M.; Trung, L.D. Future rice farming threatened by drought in the Lower Mekong Basin. *Sci. Rep.* **2021**, *11*, 15. [CrossRef] [PubMed]
45. Son, N.T.; Chen, C.F.; Chen, C.R.; Chang, L.Y.; Minh, V.Q. Monitoring agricultural drought in the Lower Mekong Basin using MODIS NDVI and land surface temperature data. *Int. J. Appl. Earth Obs. Geoinf.* **2012**, *18*, 417–427. [CrossRef]
46. Nguyen, T.T.H.; Li, M.H.; Vu, T.M.; Chen, P.Y. Multiple drought indices and their teleconnections with ENSO in various spatiotemporal scales over the Mekong River Basin. *Sci. Total Environ.* **2023**, *854*, 17. [CrossRef]
47. Dong, Z.Q.; Liu, H.; Baiyinbaoligao; Hu, H.C.; Khan, M.Y.A.; Wen, J.; Chen, L.J.; Tian, F.Q. Future projection of seasonal drought characteristics using CMIP6 in the Lancang-Mekong River Basin. *J. Hydrol.* **2022**, *610*, 11. [CrossRef]
48. Zhang, X.J.; Qu, Y.P.; Ma, M.M.; Liu, H.; Su, Z.C.; Lv, J.; Peng, J.; Leng, G.Y.; He, X.G.; Di, C.L. Satellite-Based Operational Real-Time Drought Monitoring in the Transboundary Lancang-Mekong River Basin. *Remote Sens.* **2020**, *12*, 21. [CrossRef]
49. Li, Y.S.; Lu, H.; Yang, K.; Wang, W.; Tang, Q.H.; Khem, O.H.A.; Yang, F.; Huang, Y.G. Meteorological and hydrological droughts in Mekong River Basin and surrounding areas under climate change. *J. Hydrol. Reg. Stud.* **2021**, *36*, 22. [CrossRef]
50. Wen, D.Y.; Cao, J.; Zhao, C.X.; Masiri, I.; Buntoung, S. Interdecadal variation of summer rainfall in the Greater Mekong Subregion and its possible causes. *Environ. Res. Lett.* **2021**, *16*, 9. [CrossRef]
51. Li, H.; Zhou, Y.; Wei, Y.D. Institutions, Extreme Weather, and Urbanization in the Greater Mekong Region. *Ann. Am. Assoc. Geogr.* **2019**, *109*, 1317–1340. [CrossRef]
52. Funk, C.; Peterson, P.; Landsfeld, M.; Pedreros, D.; Verdin, J.; Shukla, S.; Husak, G.; Rowland, J.; Harrison, L.; Hoell, A.; et al. The climate hazards infrared precipitation with stations-a new environmental record for monitoring extremes. *Sci. Data* **2015**, *2*, 21. [CrossRef]
53. Liang, S.L. Narrowband to broadband conversions of land surface albedo I Algorithms. *Remote Sens. Environ.* **2001**, *76*, 213–238. [CrossRef]
54. Savitzky, A.; Golay, M. Smoothing and Differentiation of Data by Simplified Least Squares Procedures. *Anal. Chem.* **1964**, *36*, 1627–1639. [CrossRef]
55. Tiwari, S.; Jha, S.K.; Sivakumar, B. Reconstruction of daily rainfall data using the concepts of networks: Accounting for spatial connections in neighborhood selection. *J. Hydrol.* **2019**, *579*, 13. [CrossRef]
56. Rodriguez, E.; Morris, C.S.; Belz, J.E. A global assessment of the SRTM performance. *Photogramm. Eng. Remote Sens.* **2006**, *72*, 249–260. [CrossRef]
57. Jones, P.G.; Thornton, P.K. Representative soil profiles for the Harmonized World Soil Database at different spatial resolutions for agricultural modelling applications. *Agric. Syst.* **2015**, *139*, 93–99. [CrossRef]
58. Cai, S.S.; Liu, D.S.; Sulla-Menashe, D.; Friedl, M.A. Enhancing MODIS land cover product with a spatial-temporal modeling algorithm. *Remote Sens. Environ.* **2014**, *147*, 243–255. [CrossRef]
59. Breiman, L. Random forests. *Mach. Learn.* **2001**, *45*, 5–32. [CrossRef]

60. Legasa, M.N.; Manzanas, R.; Calvino, A.; Gutierrez, J.M. A Posteriori Random Forests for Stochastic Downscaling of Precipitation by Predicting Probability Distributions. *Water Resour. Res.* **2022**, *58*, 17. [CrossRef]
61. Zhang, Y.F.; Liang, S.L.; Zhu, Z.L.; Ma, H.; He, T. Soil moisture content retrieval from Landsat 8 data using ensemble learning. *Isprs J. Photogramm. Remote Sens.* **2022**, *185*, 32–47. [CrossRef]
62. Tang, S.L.; Wang, H.; Feng, Y.; Liu, Q.H.; Wang, T.T.; Liu, W.B.; Sun, F.B. Random Forest-Based Reconstruction and Application of the GRACE Terrestrial Water Storage Estimates for the Lancang-Mekong River Basin. *Remote Sens.* **2021**, *13*, 4831. [CrossRef]
63. Cao, J.; Zhang, Z.; Tao, F.L.; Zhang, L.L.; Luo, Y.C.; Zhang, J.; Han, J.C.; Xie, J. Integrating Multi-Source Data for Rice Yield Prediction across China using Machine Learning and Deep Learning Approaches. *Agric. For. Meteorol.* **2021**, *297*, 15. [CrossRef]
64. Ming, W.T.; Ji, X.; Zhang, M.D.; Li, Y.G.; Liu, C.; Wang, Y.F.; Li, J.Q. A Hybrid Triple Collocation-Deep Learning Approach for Improving Soil Moisture Estimation from Satellite and Model-Based Data. *Remote Sens.* **2022**, *14*, 1744. [CrossRef]
65. Sun, X.P.; Lai, P.Y.; Wang, S.J.; Song, L.S.; Ma, M.G.; Han, X.J. Monitoring of Extreme Agricultural Drought of the Past 20 Years in Southwest China Using GLDAS Soil Moisture. *Remote Sens.* **2022**, *14*, 1323. [CrossRef]
66. Li, X.Y.; Li, Y.; Chen, A.P.; Gao, M.D.; Slette, I.J.; Piao, S.L. The impact of the 2009/2010 drought on vegetation growth and terrestrial carbon balance in Southwest China. *Agric. For. Meteorol.* **2019**, *269*, 239–248. [CrossRef]
67. Wang, M.; Ding, Z.; Wu, C.Y.; Song, L.S.; Ma, M.G.; Yu, P.J.; Lu, B.Q.; Tang, X.G. Divergent responses of ecosystem water-use efficiency to extreme seasonal droughts in Southwest China. *Sci. Total Environ.* **2021**, *760*, 14. [CrossRef]
68. Vicente-Serrano, S.M.; Begueria, S.; Lopez-Moreno, J.I. A Multiscalar Drought Index Sensitive to Global Warming: The Standardized Precipitation Evapotranspiration Index. *J. Clim.* **2010**, *23*, 1696–1718. [CrossRef]
69. Liu, Y.; Zhu, Y.; Ren, L.L.; Singh, V.P.; Yong, B.; Jiang, S.H.; Yuan, F.; Yang, X.L. Understanding the Spatiotemporal Links Between Meteorological and Hydrological Droughts From a Three-Dimensional Perspective. *J. Geophys. Res. Atmos.* **2019**, *124*, 3090–3109. [CrossRef]
70. IPCC. Summary for Policymakers. In *Climate Change 2014: Impacts, Adaptation, and Vulnerability. Part A: Global and Sectoral Aspects. Contribution of Working Group II to the Fifth Assessment Report of the Intergovernmental Panel on Climate Change*; Field, C.B., Barros, V.R., Dokken, D.J., Mach, K.J., Mastrandrea, M.D., Bilir, T.E., Chatterjee, M., Ebi, K.L., Estrada, Y.O., Genova, R.C., et al., Eds.; Cambridge University Press: Cambridge, UK; New York, NY, USA, 2014; pp. 1–32.
71. Liu, Y.X.Y.; Jing, W.L.; Wang, Q.; Xia, X.L. Generating high-resolution daily soil moisture by using spatial downscaling techniques: A comparison of six machine learning algorithms. *Adv. Water Resour.* **2020**, *141*, 22. [CrossRef]
72. Tong, C.; Wang, H.Q.; Magagi, R.; Goita, K.; Wang, K. Spatial Gap-Filling of SMAP Soil Moisture Pixels Over Tibetan Plateau via Machine Learning Versus Geostatistics. *IEEE J. Sel. Top. Appl. Earth Observ. Remote Sens.* **2021**, *14*, 9899–9912. [CrossRef]
73. Afshar, M.H.; Bulut, B.; Duzenli, E.; Amjad, M.; Yilmaz, M.T. Global spatiotemporal consistency between meteorological and soil moisture drought indices. *Agric. For. Meteorol.* **2022**, *316*, 13. [CrossRef]
74. Dorigo, W.; Himmelbauer, I.; Aberer, D.; Schremmer, L.; Petrakovic, I.; Zappa, L.; Preimesberger, W.; Xaver, A.; Annor, F.; Ardo, J.; et al. The International Soil Moisture Network: Serving Earth system science for over a decade. *Hydrol. Earth Syst. Sci.* **2021**, *25*, 5749–5804. [CrossRef]
75. Peng, J.; Niesel, J.; Loew, A.; Zhang, S.Q.; Wang, J. Evaluation of Satellite and Reanalysis Soil Moisture Products over Southwest China Using Ground-Based Measurements. *Remote Sens.* **2015**, *7*, 15729–15747. [CrossRef]
76. Sun, H.; Xu, Q. Evaluating Machine Learning and Geostatistical Methods for Spatial Gap-Filling of Monthly ESA CCI Soil Moisture in China. *Remote Sens.* **2021**, *13*, 2848. [CrossRef]
77. Liu, X.L.; Richardson, A.G. Edge deep learning for neural implants: A case study of seizure detection and prediction. *J. Neural Eng.* **2021**, *18*, 16. [CrossRef]
78. Yu, J.X.; Zhang, X.; Xu, L.L.; Dong, J.; Zhangzhong, L.L. A hybrid CNN-GRU model for predicting soil moisture in maize root zone. *Agric. Water Manag.* **2021**, *245*, 10. [CrossRef]
79. Zhao, H.F.; Li, J.; Yuan, Q.Q.; Lin, L.P.; Yue, L.W.; Xu, H.Z. Downscaling of soil moisture products using deep learning: Comparison and analysis on Tibetan Plateau. *J. Hydrol.* **2022**, *607*, 20. [CrossRef]
80. Karthikeyan, L.; Mishra, A.K. Multi-layer high-resolution soil moisture estimation using machine learning over the United States. *Remote Sens. Environ.* **2021**, *266*, 19. [CrossRef]
81. Keovilignavong, O.; Nguyen, T.H.; Hirsch, P. Reviewing the causes of Mekong drought before and during 2019–20. *Int. J. Water Resour. Dev.* **2021**, *21*, 155–175. [CrossRef]
82. Guo, H.; Bao, A.M.; Liu, T.; Ndayisaba, F.; He, D.M.; Kurban, A.; De Maeyer, P. Meteorological Drought Analysis in the Lower Mekong Basin Using Satellite-Based Long-Term CHIRPS Product. *Sustainability* **2017**, *9*, 901. [CrossRef]
83. Liu, B.J.; Liang, M.L.; Huang, Z.Q.; Tan, X.Z. Duration-severity-area characteristics of drought events in eastern China determined using a three-dimensional clustering method. *Int. J. Climatol.* **2021**, *41*, E3065–E3084. [CrossRef]
84. Sein, K.K.; Chidthaisong, A.; Oo, K.L. Observed Trends and Changes in Temperature and Precipitation Extreme Indices over Myanmar. *Atmosphere* **2018**, *9*, 477. [CrossRef]
85. Zaki, M.K.; Noda, K. A Systematic Review of Drought Indices in Tropical Southeast Asia. *Atmosphere* **2022**, *13*, 833. [CrossRef]
86. Nagaraj, D.; Proust, E.; Todeschini, A.; Rulli, M.C.; D'Odorico, P. A new dataset of global irrigation areas from 2001 to 2015. *Adv. Water Resour.* **2021**, *152*, 8. [CrossRef]
87. FAO. *World Food and Agriculture—Statistical Yearbook 2021*; FAO: Rome, Italy, 2021; 368p.

88. Mishra, A.; Ketelaar, J.W.; Uphoff, N.; Whitten, M. Food security and climate-smart agriculture in the lower Mekong basin of Southeast Asia: Evaluating impacts of system of rice intensification with special reference to rainfed agriculture. *Int. J. Agric. Sustain.* **2021**, *19*, 152–174. [CrossRef]
89. Thilakarathne, M.; Sridhar, V. Characterization of future drought conditions in the Lower Mekong River Basin. *Weather Clim. Extrem.* **2017**, *17*, 47–58. [CrossRef]
90. Kreibich, H.; Van Loon, A.F.; Schroter, K.; Ward, P.J.; Mazzoleni, M.; Sairam, N.; Abeshu, G.W.; Agafonova, S.; AghaKouchak, A.; Aksoy, H.; et al. The challenge of unprecedented floods and droughts in risk management. *Nature* **2022**, *608*, 80–86. [CrossRef]